DOI 10.4430/bgo00434

A comparative study of GPR data processing based on Compensated Time-Reversal and Time-Reversal imaging

S. Ghanbari[1], M.K. Hafizi[2], M. Bano[3], A. Ebrahimi[4] and J. Webb[5]

[1] *Faculty of Science, Razi University, Kermanshah, Iran*
[2] *Institute of Geophysics, University of Tehran, Tehran, Iran*
[3] *Ecole et Observatoire Université de Strasbourg, Strasbourg, France*
[4] *Department of Computer Science and Information Technology, La Trobe University, Melbourne, Australia*
[5] *Department of Ecology, Environment and Evolution, La Trobe University, Melbourne, Australia*

(Received: 9 October 2022; accepted: 20 September 2023; published online: 30 November 2023)

ABSTRACT To improve the resolution of ground penetrating radar (GPR) signals, the Compensated Time-Reversal (CTR) method is applied, especially in lossy media, where the conventional time reversal method has the negative effect of dispersion and loss in the propagation medium. To create the CTR method, Time-Reversal (TR) processing combined with attenuation compensation based on continuous wavelet transform is applied. The application of both the TR and CTR methods to synthetic data showed a significant improvement of the radargram resolution, effectively differentiating anomalies within a low-loss medium, especially when the latter approach was implemented. To test the method in a real-world situation, a forensic GPR investigation was carried out to detect the body of a climber buried by a snow avalanche in the Karkas Mountains, Natanz, Iran. Both the TR and CTR methods successfully located the body, but the CTR method provided better definition of both the body and nearby reflectors related to the subsurface features like specific layers of snow. These results demonstrate that the CTR application is efficient at enhancing the spatial resolution of GPR radargrams and proves to have substantial promise as a GPR processing technique, although the method is relatively time consuming.

Key words: TR technique, CTR, forensic GPR, CWT, data processing.

1. Introduction

Ground Penetrating Radar (GPR) is a robust and widely applicable method in near surface engineering. This technique is generally used to non-destructively detect concealed concrete, metallic, and plastic targets such as tubes, drums, and pipes (Ebrahimy *et al*., 2012; Ghanbari and Hafizi, 2016; Sun *et al*., 2019). Further, it can also be used to implement efficient surveys of forensic geophysics in diverse conditions, including the detection of buried bodies (Forbes *et al*., 2013; Barone and Maggio, 2018, 2019). Traditional GPR data processing techniques, which typically follow procedures used in electromagnetic (EM) and seismic data processing, do not always yield good results in improving the resolution of radargrams and suppressing noise. The issue occurs due to ground clutter, ground losses, and geological anomalies, that regularly obscure the target response (Ebrahimi *et al*., 2017; Jazayeri *et al*., 2017; Santos and Teixeira, 2017).

Technically speaking, the signal behaviour can vary according to the individual environments surveyed; factors like humidity and compactness of subsurface layers can surprisingly affect the shape of the reflected signal.

As a result, advanced methods of signal processing are required. The microwave imaging method (introduced to detect and localise objects) combined with the Time-Reversal (TR) technique (Fink *et al*., 2000) has shown promise. The TR technique is based on the invariance of Maxwell's equations with respect to time, in that there is a time reversed wave that back propagates into the medium and automatically focuses on reflective targets and anomalies. This technique is well-defined in lossless and approximately low-loss media; it was initially applied to acoustics (Fink *et al*., 1989; Fink, 1992), followed by non-destructive testing (Liu *et al*., 2014), sound quality enhancement (Lin and Too, 2014), atmospheric studies (Mora *et al*., 2012), and subsurface geophysics (Artman *et al*., 2010; Yavuz *et al*., 2014; Chen *et al*., 2016; Santos and Texeira, 2017; Bradford *et al*., 2018).

From a practical point of view, TR achieves super-resolution by utilising multipath wave propagation in the medium (Fouda *et al*., 2012). Nevertheless, if invariance of the wave equations is broken in a dispersive medium, the TR microwave imaging technique is impacted by losses (Yavuz and Teixeira, 2005). The additional phase shift, caused by dispersion, can be compensated by the TR process itself (Yavuz and Teixeira, 2006). However, the attenuation, which influences the signals in the forward and backward propagation steps, is not rectified, and ultimately reduces the focusing localisation resolution. Therefore, although TR imaging can enhance the radargram resolution, especially in lossy media, there is a negative effect of dispersion and loss in the propagation medium. The earliest work on the compensation of this attenuation used the Short-Time Fourier Transform method, which takes frequency dependency into account to improve the resolution (Yavuz and Teixeira, 2006). More recently, continuous wavelet transformation has been applied to tackle the invariance degradation of the wave equations, caused by attenuation. This was performed by utilising an inverse filter in the wavelet domain to enhance the focusing resolution; this algorithm was successfully applied to the localisation of lung cancer (Abduljabbar *et al*., 2017). Similarly to other methods used in seismic studies to extend wavefields, Reverse Time Migration (RTM) consists of two main stages: wavefield extrapolation and the application of an imaging condition. In the case of post-stack (zero-offset) RTM, wavefield extrapolation involves propagating the stacked data backwards. However, for pre-stack RTM, the process of wavefield extrapolation is divided into two substeps. The first substep involves forward extrapolation, which combines the source wavefield at each time pattern. The second substep involves back propagation of the surface recorded data to reconstruct the reflected wavefield at each time sample (Yao, 2013). In seismic imaging applications, RTM was used to extrapolate the received EM field into subsurface layers. This extrapolation was achieved by solving Maxwell's equations with a negative time step, while the waves were generated from the time-reversed stacked or zero-offset section, which functioned as a surface boundary condition. In the case of post-stack RTM, the imaging condition is satisfied when the clock reaches zero. At this point, all the recorded energy is injected back into the model and propagated downwards to its original source. The researchers employed the decoupled, second-order differential form of Maxwell's equations, which simplifies to the damped scalar wave equation in 2D when the electric field is polarised perpendicularly to the image plane (Bradford *et al*., 2018).

To evaluate the performance of these attenuation-compensation methods, it is appropriate to select a low-loss environment such as ice and snow. GPR has frequently been utilised to investigate ice structures and snow properties (Bradford *et al*., 2009; Galley *et al*., 2009; Annan *et al*., 2016), and could also be used to locate people buried by snow avalanches.

A new comparative processing approach to GPR data is presented in this paper. The approach was tested by detecting a climber's body buried in snow (a low-loss medium) on the slopes of the Karkas Mountains, near Natanz, Iran. We initially defined a synthetic model to study the behaviour of a wave with a typical 250 MHz central frequency and considered a synthesised buried body as the target. This was, then, applied to the real situation using two versions of advanced GPR processing: TR imaging, and a modified TR algorithm, hereafter called Compensated Time-Reversal (CTR), combining attenuation compensation based on continuous wavelet transform with conventional software-based processing of the GPR radargrams (Ghanbari *et al*., 2021). Hereinafter, the results will be sequentially discussed, with the technical aspects elaborated when each method lost the power to explore anomalies (climber's body, subsurface layers, and snowy overburden).

2. Methodology

To elaborate the CTR, firstly, we need to understand the concept of the TR technique. The TR technique comprises four steps (Fig. 1): 1) a pulse signal is initially emitted from transceivers (Fig. 1a); 2) the emitted signal propagates through the dominant medium and is, consequently, reflected by some targets (Fig. 1b); 3) the reflected signals are collected by the transceivers (Fig. 1c); and, 4) the received signals are, finally, reversed in time and sent back through the medium (Fig. 1d). Back-propagation can occur either physically, in a laboratorial way, or, when possible, through receivers/transmitters placed in the medium of the wave propagation. In the latter case, the processes of sending and receiving waves are directly performed by using receivers/transmitters. Evidently, such conditions are not available in most geophysical studies. Conversely, back-propagation can be synthetically carried out by means of a forward simulation engine, such as the Finite-Difference Time-Domain method (Santos and Texeira, 2017). When a signal propagates through a dispersive and lossy medium, acting as a low-pass filter, the invariance of the wave equations is broken, and the signal suffers from attenuation. For this reason, inverse filters are required for compensation. During the forward propagation of the signal, the

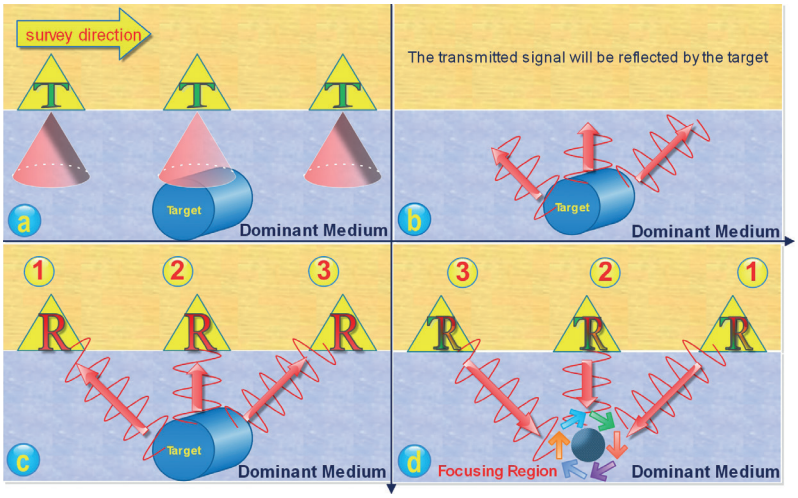

Fig. 1 - TR technique steps: a) transmitting, b) reflecting, c) receiving, d) reversing and sending back (Bradford *et al*., 2018).

real part of the dielectric permittivity (ε) of the medium causes a phase shift to the traveling waves. According to the TR concept, the back-propagated signal is coherently phase-conjugated along all bandwidths, so that the phase shift is inherently corrected (Yavuz and Texeira, 2009; Abduljabbar *et al*., 2016; Ghanbari *et al*., 2022a). Nonetheless, the presence of an imaginary component within the dielectric permittivity contributes to signal attenuation. Within a medium that attenuates signals, this attenuation is dependent on both the signal frequency and the time required for the signal to propagate through the medium.

To overcome the problem of attenuation, Abduljabbar *et al*. (2017) proposed a method using the Continuous Wavelet Transform (CWT) technique, which incorporates both time and frequency variations for microwave propagation. A similar method is used here to compare the GPR signals of TR imaging outcomes with and without an attenuation compensation filter based on CWT.

Following the above-mentioned methodology, the Morlet wavelet (Morlet *et al*., 1982; Braga and Moraes, 2013) has been chosen for analysing the propagated wave in attenuating and dispersive media. The wavelet in a time domain is defined as (Torrence and Compo, 1998):

$$\Psi_0[n] = \frac{1}{\sqrt[4]{\pi}} e^{jf_{cm}n\Delta t} e^{-\frac{(n\Delta t)^2}{2}} \tag{1}$$

where n is the time index, Δt is the time step in seconds, j is the imaginary unit and f_{cm} is the central frequency of the mother wavelet. In a scaled-frequency domain $\Psi_0[n]$ is given as:

$$\Psi_0(a_j\omega_k) = \frac{1}{\sqrt[4]{\pi}} e^{-\frac{(a_j\omega_k - f_{cm})^2}{2}} \tag{2}$$

where a_j is the dimensionless scaling as $a_j = a_0 2^{j\Delta}$ for $j = 0.1, ..., S-1$, a_0 is the smallest scale, and S is the largest scale S = ceiling function $\left[\frac{1}{\Delta_j}\log_2\left(\frac{N\Delta t}{a_0}\right)\right]$. N is the number of samples in the time domain signal, k is the frequency index and ω_k is the angular frequency given by (Torrence and Compo, 1998):

$$\omega_k = \begin{cases} 0 & k = 1 \\ \frac{2\pi k}{N\Delta t} & 1 < k \leq \frac{N}{2} + 1 \\ -\frac{2\pi k}{N\Delta t} & \frac{N}{2} + 1 < k \leq N \end{cases} \quad \text{for } k = 1, 2, \ldots, N; \text{ and } \Delta j = \Delta t = 0.025 .$$

A flexible set of scales can be employed to enhance the precision of the representation. In the context of the Morlet wavelet, which is a nonorthogonal wavelet, a Δj value of up to 0.5 is considered sufficient for achieving adequate sampling across various scales. Opting for smaller Δj values offers a higher level of resolution and detail in the analysis. To attain optimal results, the selection of both Δj and Δt (as proposed by Torrence and Compo, 1998) is combined with trial-and-error-based exploration of different values at each step.

Generally, a wavelet should be admissible, and this can be realised when (Farge, 1992):

$$\lim_{N\to\infty} \sum_{n=-N}^{N} \Psi_0[n] = 0 \quad \text{and} \quad \Psi_0(a_j\omega_k) = \begin{cases} \frac{1}{\sqrt[4]{\pi}} e^{-\frac{(a_J\omega_k - f_{cm})^2}{2}} & \omega_k > 0 \\ 0 & \omega_k \leq 0. \end{cases} \tag{3}$$

To start the compensation method, the CWT of the observed signal $x[n]$ is represented as:

$$X[n,a_j]=\sum_{k=1}^{N}\left\{\sum_{j=1}^{N}x[i]e^{-j\frac{2\pi}{N}ik}\Psi^{*}(a_j\omega_k)\right\}e^{j\frac{2\pi}{N}nk}. \quad (4)$$

To create an inverse filter, attenuation must be calculated first. The next step is to compensate the attenuation by applying the inverse filter to $X[n, a_j]$ in the wavelet domain. For plane wave propagation, the solution of Maxwell's equations in a dispersive medium (Taflove and Hogness, 2005) is:

$$E[n]=e^{j2\pi fn\Delta t}e^{-j2\pi f\sqrt{\varepsilon\mu}d[n]} \quad (5)$$

that can be written as:

$$E[n]=e^{j2\pi fn\Delta t}e^{-j2\pi f\sqrt{\varepsilon_r}\frac{d[n]}{C}}=e^{j2\pi fn\Delta t}e^{-j2\pi f\boldsymbol{Re}[\sqrt{\varepsilon_r}]\frac{d[n]}{C}}e^{2\pi f\boldsymbol{Im}[\sqrt{\varepsilon_r}]\frac{d[n]}{C}}\triangleq e^{J2\pi fn\Delta t}\Theta\Gamma \quad (6)$$

where f is the frequency; j is the imaginary unit; $d[n]$ is the distance between the excitation and observation, which is contingent upon the propagation of waves through a medium; $\mu = \mu_0\mu_r$ is the magnetic permeability of the medium, μ_0 is the free space magnetic permeability, and μ_r is the relative magnetic permeability of the dispersive medium; $\varepsilon = \varepsilon_0\varepsilon_r$ is the permittivity of the medium; ε_0 is the free space permittivity; ε_r is the complex relative permittivity of medium; $C=\frac{1}{\sqrt{\varepsilon_0\mu_0}}$ is the speed of light in the vacuum; **Re** $[\sqrt{\varepsilon_r}]$ and **Im** $[\sqrt{\varepsilon_r}]$ are the real and imaginary parts of $\sqrt{\varepsilon_r}$; Γ is the attenuation, and Θ is the phase shift defined as:

$$\Gamma[n,f]=e^{2\pi f\boldsymbol{Im}[\sqrt{\varepsilon_r}]\frac{d[n]}{C}} \quad \text{and} \quad \Theta[n,f]=e^{-\mathrm{j}2\pi f\boldsymbol{Re}[\sqrt{\varepsilon_r}]\frac{d[n]}{C}}. \quad (7)$$

The inverse filter extracted from the above equation is:

$$H[n,a_j]=\frac{1}{\Theta[n,a_j].\Gamma[n,a_j]}=e^{j2\pi\frac{f_c}{a_j}\boldsymbol{Re}[\sqrt{\varepsilon_r}]\frac{d[n]}{C}}e^{-2\pi\frac{f_c}{a_j}\boldsymbol{Im}[\sqrt{\varepsilon_r}]\frac{d[n]}{C}} \quad (8)$$

where a_j is a scaling factor, which controls the actual frequency, and f_c is the central frequency of $x[n]$. H should be stabilised (Wang, 2006) as:

$$H_s[n,a_j]=\frac{\Gamma[n,a_j]}{\Gamma[n,a_j]^2+T}.\frac{1}{\Theta[n,a_j]}. \quad (9)$$

T denotes the stabilisation factor, which remains constant in all the simulations. The stabilised compensated wave, $Y[n, a_j]$, is:

$$Y[n,a_j]=X[n,a_j]H_s[n,a_j]. \quad (10)$$

Ultimately, by applying the Inverse Continuous Wavelet Transform to $Y[n,a_j]$, the compensated signal will be obtained as (Torrence and Compo, 1998):

$$X_c[n] = \frac{1}{C_\delta}\sum_{j=1}^{J}\frac{\Re\left[Y[n,a_j]\right]}{\sqrt{a_j}} \tag{11}$$

where

$$C_\delta = \sum_{j=1}^{J}\frac{\Re\left[X_\delta[a_j]\right]}{\sqrt{a_j}},$$

and for the Morlet wavelet, the CWT of a delta function is calculated as:

$$X_\delta[a_j] = \frac{1}{N}\sum_{k=1}^{N}\Psi^*(a_j\omega_k). \tag{12}$$

Fig. 2 shows the steps in the conventional TR and CTR processes defined above, applied to a set of GPR data.

One of the most important issues in GPR studies is the estimation of velocity so as to convert time to depth in order to estimate the thickness of the layers; the velocity (v) is determined by the relative dielectric permittivity (ε_r) and the free space EM velocity (C = 0.3 m/ns), as follows (Ulaby *et al.*, 2010):

$$v = \frac{C}{\sqrt{\varepsilon_r}}. \tag{13}$$

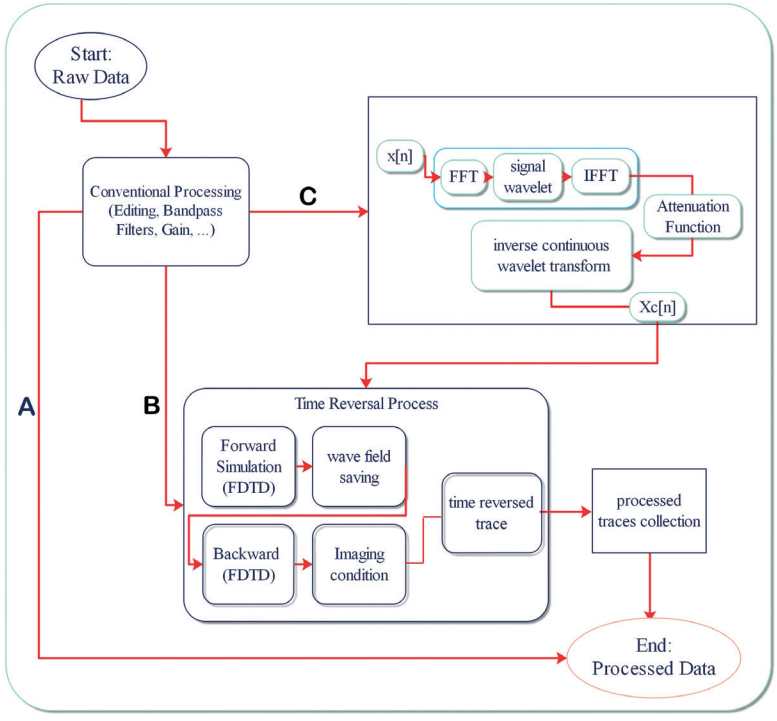

Fig. 2 - A model for GPR signal processing by employing processing approaches including conventional processing (denoted by A), TR [indicated by B; based on Liu *et al.* (2014) and Santos and Teixeira (2017)] and CTR approach [based on Abduljabbar *et al.* (2017) and Ghanbari *et al.* (2022b)].

3. Synthetic model

Firstly, TR and CTR are applied to a designed model. The TR imaging technique is based on wave propagation in a loss-less propagation media that cannot be experienced in real life. In comparison, to create the compensation filter, CTR only requires complex permittivity at the central frequency of the dominant medium. Hence, the choice of a medium with low attenuation is appropriate. Snow is a suitable choice, and its dielectric permittivity plays an essential role in the implementation of the attenuation compensation method.

Here, snow is classified according to its volumetric water content or wetness (*W*): dry (*W* = 0.00), moist (*W* = 0.00-0.03), wet (*W* = 0.03-0.08), very wet (*W* = 0.08-0.15), and slush (*W* > 0.15) (Green *et al*., 2004; Braford *et al*., 2009). At low wetness, liquid water in snow exists as isolated water bodies in the pores (pendular regime); with increased wetness, the water droplets join to form continuous liquid paths through the connected pore spaces (funicular regime). Wet snow is included in the pendular regime (Denoth, 2003). Dry snow is a two-component system, made of air and ice that behaves like an insulating material opposing the flow of electrical current by high electrical resistivity. On the contrary, wet snow can be considered as a three-phase mixture composed of air, ice, and water. Therefore, there is a fundamental difference between wet and dry snow (Colbeck, 1997; Arslan *et al*., 2001). The dielectric permittivity of dry snow is determined by the density, but the dielectric permittivity properties of wet snow depend on the water content because of the large permittivity contrast between ice and liquid water. The increase in both the real and imaginary parts of the complex dielectric permittivity of wet snow has the same volumetric wetness dependence, and the frequency dependence of the complex dielectric permittivity of wet snow is the same as that of water (Tiuri *et al*., 1984).

There are many experimental measurements of the relative dielectric permittivity of wet snow but the results for the imaginary part are contradictory. Some of the discrepancies are due to the difficulties in determining the liquid water content and the inhomogeneity of snow. Moreover, worthy of consideration are certain situations, such as the occurrence of avalanches, that can lead to alterations in the dielectric permittivity properties.

The relationships between the complex dielectric permittivity of snow and its liquid water content and density are expressed by a set of empirical equations (Sihvola and Tiuri, 1986):

$$\varepsilon'_d = (1 + 1.7\rho_d + 0.7\rho_d^2) \tag{14}$$

$$\varepsilon'_s = (0.10W + 0.80W^2)\varepsilon'_w + \varepsilon'_d \tag{15}$$

$$\varepsilon''_s = (0.10W + 0.80W^2)\varepsilon''_w \tag{16}$$

where ε'_d, ε'_s, and ε''_s indicate, respectively, the dielectric permittivity of dry snow and the real and imaginary parts of the complex dielectric permittivity of wet snow, *W* is snow wetness by volume, ρ_d is the equivalent dry snow density in g/cm^3, and the subscripts *w, s*, and *d* indicate the properties of water (*w*), wet snow (*s*) and dry snow (*d*), respectively. These equations are valid to a good approximation for the frequency band range from 10 MHz to 1.5 GHz.

A GPR signal propagating through snow follows a frequency-dependent attenuation pattern. ε'_s is approximately independent of frequency but strongly depends on *W*. Conversely, the attenuation is primarily a function of ε''_s (which increases rapidly with frequency) and *W* (Bradford *et al*., 2009). The frequency dependence of ε''_s in wet snow follows the frequency

dependence of water, ε''_w (Turner and Siggins, 1994).

To qualitatively test the CTR imaging, we built a simple two-layer model, 5 m × 10 m in the *X* and *Y* directions, respectively (Fig. 3). Table 1 provides a comprehensive description of the media employed in the models, along with their respective physical properties. It is noteworthy that all media considered in the study exhibit a uniform value of μ = 1. In Fig. 3, the 0.2-metre-thick upper layer (light blue) is composed of fresh snow with a relative dielectric permittivity of 2, and conductivity of 5 µS/m. This layer is considered only as a distinguisher. The underlying 9-metre layer (blue) represents compact old snow with a mean relative real dielectric permittivity of 2.82, and mean conductivity of 100 µS/m. A buried body was included in the model as two anomalies of biological tissues, one for the head and one for the main part of the body. Biological tissues present relatively high electrical conductivity, which means diagnostic features for the GPR imaging of human bodies are restricted to the surrounding medium, skin interface, and shallow tissue interfaces. A shadow zone with low amplitude reflection occurs beneath a body due to high GPR attenuation within the body (Hammon III *et al*., 2000). The model presents two biological anomalies, both embedded in the second layer of snow. The first one for the head [dark blue circle centred on *X* = 3.2 m, *Z* =1 m (Fig. 3)] has a dielectric permittivity of 60, and conductivity of 0.9 S/m. The second anomaly for the main part of the body (demonstrated through a box depicted in Fig. 3) has approximate average values for the physical parameters of body tissues (Schwan and Li, 1953; Pethig, 1985; Gabriel *et al*., 1996a, 1996b).

Table 1 - Overview of media used in the models and their selected physical characteristics based on Hammon III *et al.* (2000).

Media	**First layer of snow (distinguisher)**		**Main propagating media (snow)**					**Head of body (circle)**		**Body (rectangle)**	
Properties	σ (µS/m)	ε	σ (µS/m)	ε'_s	ε''_s	ρ (g/cm^3)	W	σ (S/m)	ε	σ (S/m)	ε
	5	2	100	2.82	0.012	0.39	0.08	0.9	60	0.6	40

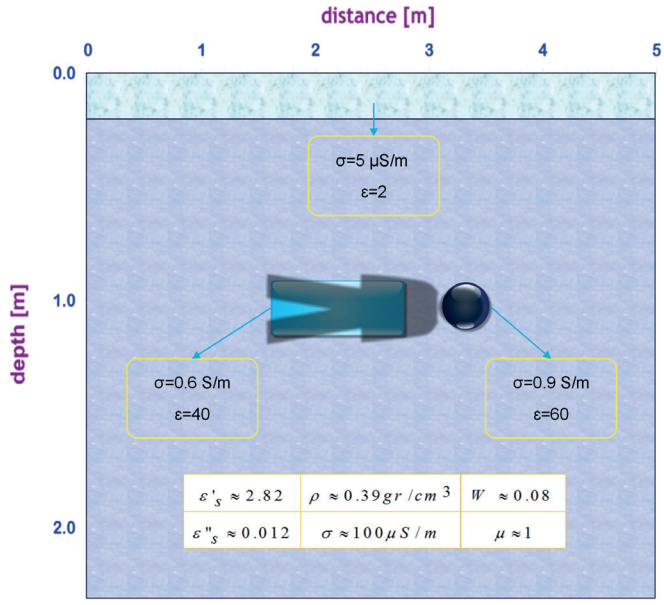

Fig. 3 - A schematic representation of a body buried in snow, showing overburden and lower layers, target, and physical parameters. The dark circle indicates the area of the head, with higher conductivity and dielectric permittivity, while the rest of the body (rectangular box) was modelled using lower parameters.

A 2D time migration mode finite-difference time-domain solution was employed using Maxwell's equations, a grid size of 0.005 m, an excitation source that is a Ricker wavelet with central frequency of 250 MHz, a time sampling interval of 0.005 ns, and a dominant medium velocity of 0.18 m/s. In Fig. 4a, the calculated synthetic radargram displays three hyperbolic events occurring within a 10 ns timeframe (at X~ 1.6 m, 2.8 m, and 3.2 m). The two hyperbolic events on the left correspond to the sides of the rectangle, while the third event is associated with the circle. These reflections, with relatively low amplitudes, are all situated within the buried object. After applying pre-processing procedures (move start time, dewow, gain function, background removal, bandpass frequency filtering) to the first radargram, the hyperbolic events presented higher amplitudes and better appearance (Fig. 4b). TR and CTR processing (Figs. 4c and 4d) differentiated the anomalies (indicated with red boxes) more clearly, but the use of CTR provided greater appearance with higher amplitudes of the anomalies in the radargram.

4. Field application: data acquisition

The synthetic modelling demonstrated that CTR processing of a radargram can locate a body buried in snow. To verify the applicability in the real world, this technique was used to search for a climber buried by a snow avalanche in proximity of the summit of the Karkas Mountains, near Natanz city, Iran. The climbers who had accompanied the lost climber provided indication

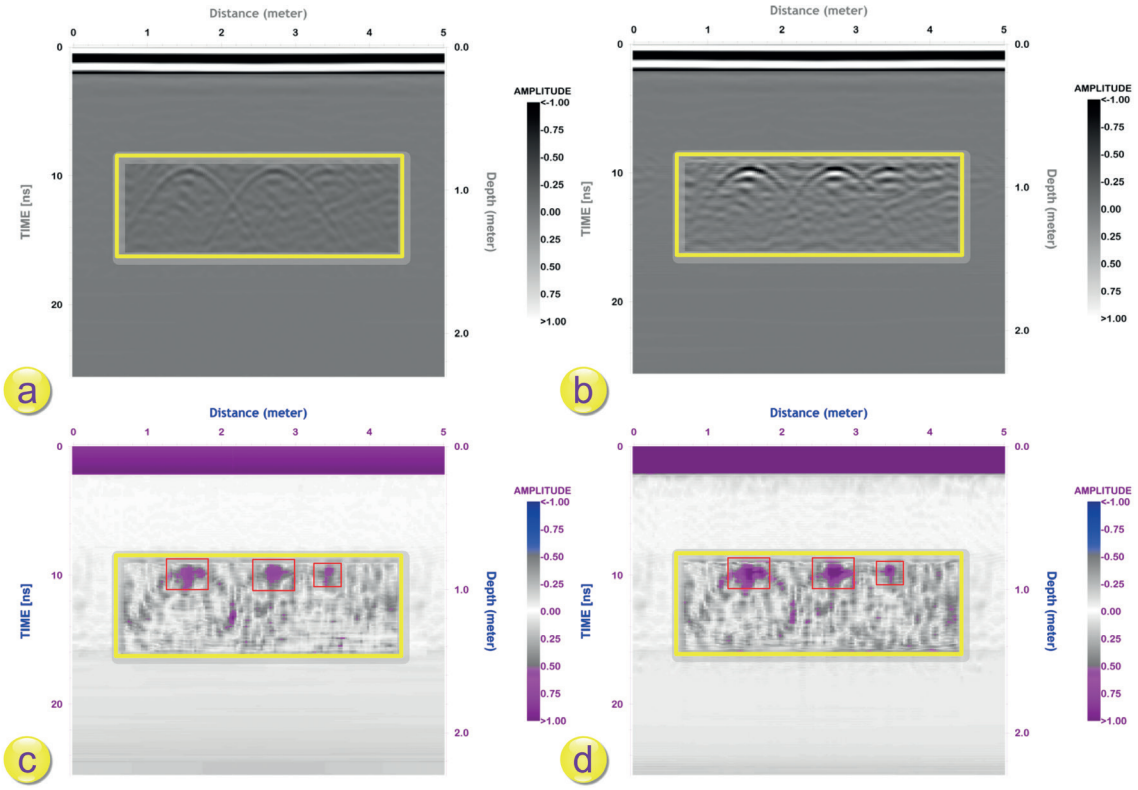

Fig. 4 - A computed synthetic model: a) raw radargram, b) processed data, c) after application of TR processing, d) after application of CTR. The yellow rectangle indicates the buried body; the red boxes show the anomalies.

of his approximate location prior to the avalanche, and, from the direction of the avalanche, a small valley, close to the initial position of the climber, was determined to be a probable site for locating the body.

The data was acquired using a MALA GPR system with an antenna central frequency of 250 MHz. Fig. 5 displays the location of the data acquisition campaign site and its surroundings. The team encountered challenges as a result of the extreme elevation (3800 m a.s.l.), and difficult topography, and time limitations, which posed restrictions on the implementation of 3D data acquisition. Carrying out short test surveys within the valley luckily identified a poorly defined target. Three detailed transects (Fig. 6) were, then, conducted; the L2 and L3 parallel transects were approximately one metre apart and crossed L1, which was acquired along the long axis of the climber's body.

Fig. 5 - The data acquisition campaign comprising a view of the Karkas Mountains, field operation, design, data acquisition, and velocity measurements/tests for the travel time-to-depth conversion (panels a to d).

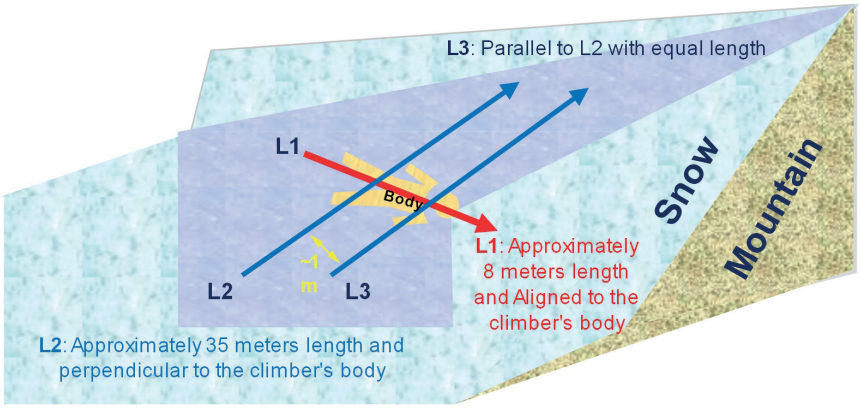

Fig. 6 - Scheme of how the transect lines (L1, L2, and L3) are placed versus the position of the climber's body. Lines L2 and L3 are approximately 1 m apart.

5. Field application: processing and interpretation

To convert travel time to depth, velocity must be calculated. This was achieved by using the mean complex dielectric permittivity of snow determined from Eqs. 13 to 16, and related parameters, such as the density of wet snow. The average calculated velocity based on this

method was 0.18 m/s. It was calibrated by converting the time axis to depth using the move out analysis of diffraction hyperbolas explained in the Appendix (Bradford and Harper, 2005), and point measurements of snow depth using a probe (e.g. Marshall *et al*., 2005).

The data acquired was processed by REFLEXW software (Sandmeier, 2012), with some pre-processing and initial processing steps: move start time, dewow, gain function, background removal, and bandpass frequency filtering (Figs. 7a, 8a, and 9a). A topography correction was, then, applied (Figs. 7b, 8b, and 9b); this showed a relatively good contrast between the snow and underlying rock but there were no obvious signs of the body. The fact that the expected reflectors were significantly attenuated or dampened was probably due to the body's irregular shape and to it being covered by mountaineering clothing.

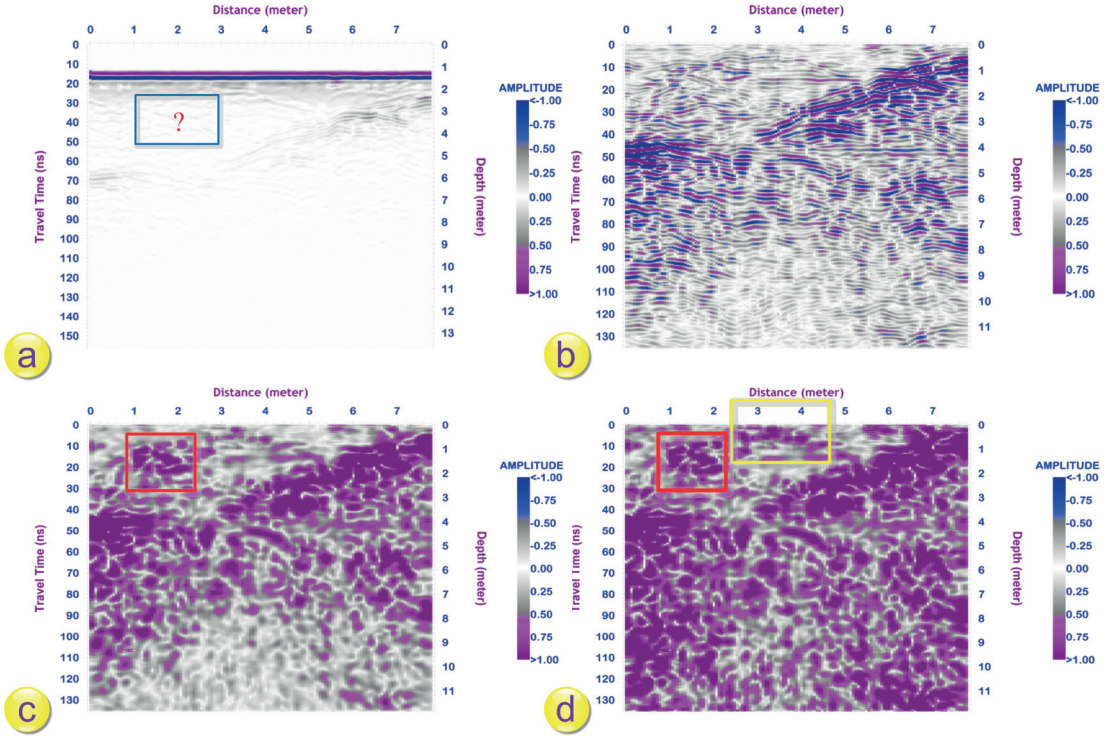

Fig. 7 - L1 radargrams: a) raw data, b) conventionally processed data, c) TR after application, d) CTR after application. The blue box indicates the probable location of the climber's body; the red box indicates the location of the buried body; the yellow box indicates another anomaly discussed in the text. To make comparison easier, the amplitude intensity of the radargrams has been matched.

Application of TR in a trace-by-trace manner (Figs. 7c, 8c, and 9c) showed a substantial improvement of the radargram resolution, and, in particular, the detection of reflected waves from the body on transects L1 and L2 at a depth of approximately 1 m (red box). In addition, other anomalies were present but not clearly delineated (yellow boxes, discussed further below). Application of CTR (Figs. 7d, 8d, and 9d) showed that the utilisation of this method has the potential to enhance the quality of radargrams and reduce wave attenuations. Thus, more reflections became visible from the body, particularly for transect L3 (Fig. 9c), while for transect L1 the waves emitted from the body presented more intense amplitudes compared to the TR

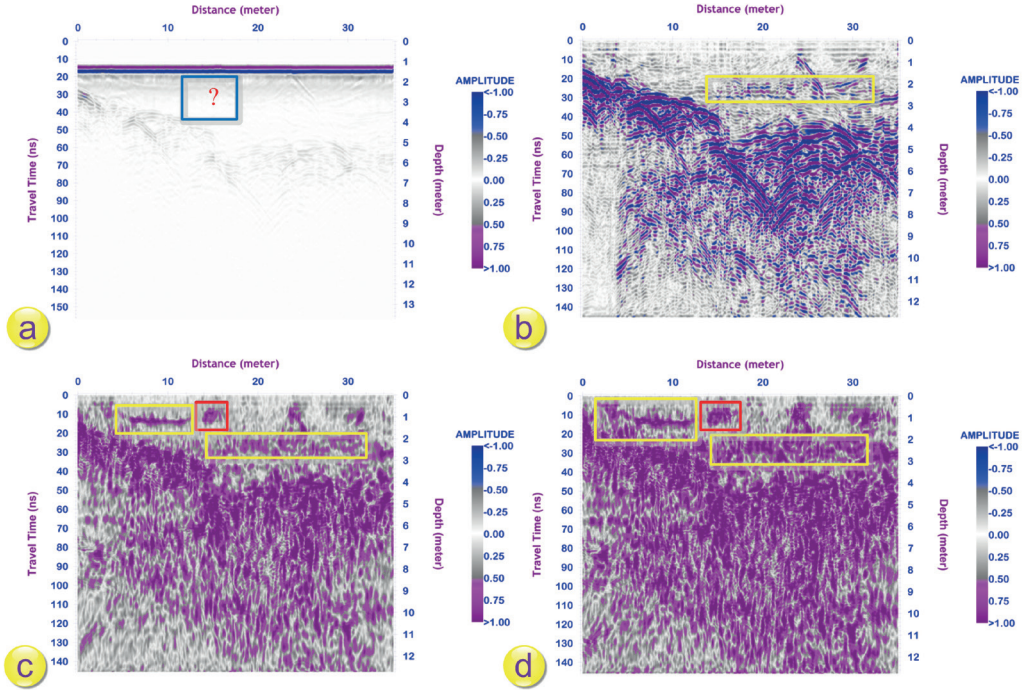

Fig. 8 - L2 radargrams, a) raw data, b) conventionally processed data, c) TR after application, d) CTR after application. The blue box indicates the probable location of the climber's body; the red box indicates the location of the buried body; the yellow boxes indicate other anomalies discussed in the text.

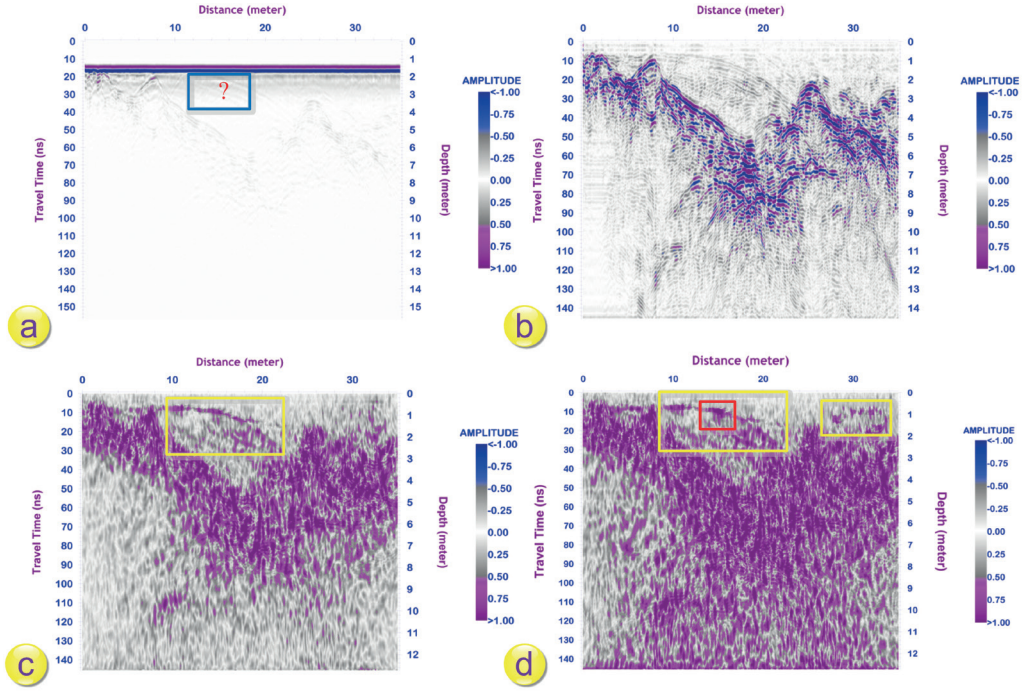

Fig. 9 - L3 radargrams, a) raw data, b) conventionally processed data, c) TR after application, d) CTR after application. The blue box indicates the probable location of the climber's body; the red box indicates the location of the buried body; the yellow boxes indicate other anomalies (see text for discussion).

radargram (Fig. 7c). A better definition of the anomalies within the yellow boxes is also evident, allowing some to be identified as specific layers of snow; other anomalies may arise from the presence of rocks or mountaineering equipment.

The Signal-to-Noise Ratio (SNR) is used to qualitatively compare the TR and CTR values. SNR is the ratio of the signal energy and noise energy (Petromichelakis *et al.*, 2018). To perform this comparison the specific portion of the radargrams containing the primary object (mountaineer body) was selected based on its approximate location. From a technical standpoint, traces numbered 290 to 320 were averaged. The SNR results for the related radargrams are shown in Table 2.

Table 2 - Summary of the SNR radargram analysis results after TR and CTR application.

Processing method	SNR (db.)			Comments on the outcomes of each processing technique.
	L1	L2	L3	
Traditional processing	11	11	11	The boundary of the overburden/snow layer and rocks was determined; however, no evidence of the buried body was found.
TR imaging	16	15	15	Compared to the traditional processing, a better resolution and contrast between subsurface layers was obtained, and some footprints of the target/buried body appeared.
CTR imaging	19	18	19	Compared to TR, CTR revealed a higher resolution and better SNR, especially in focus regions, a better contrast of the subsurface layers, the appearance of new anomalous area, and more precise target detection.

The SNR indicates that the CTR results are better than the TR results. TR outcomes are also better when compared to those obtained with the conventional processing method. Following the completion of the GPR survey, excavation at the site verified the location of the climber's body, as shown on the transects.

6. Conclusions

To improve the resolution of GPR radargrams, TR processing was combined with attenuation compensation to create the modified CTR method. Both the TR and CTR methods can effectively differentiate anomalies within a low-loss medium, as shown by their successful location of a body buried in snow (the identification of the detected target is inferred from the excavations and corresponding interpretations) using both synthetically modelled data and a real-world situation, where a climber had been buried by a snow avalanche. The TR imaging method detected the position of the buried body but failed to clearly delineate nearby anomalies. CTR provided a better definition of both the body and nearby reflectors related to subsurface features, such as specific layers of snow. Therefore, CTR proves to be a substantial promise as a GPR processing technique, although it is relatively time consuming.

Acknowledgments. I would like to acknowledge the Institute of Geophysics, University of Tehran, Iran, for their generous support during my PhD program, and my sincere appreciation to all those involved in the fieldwork, as well as the ZAP Consulting Engineers Company. My sincere thanks also go to the Ecole et Observatoire Université de Strasbourg for offering me the opportunity to work in person with Maksim Bano.

REFERENCES

Abduljabbar A.M., Yavuz M.E., Costen F., Himeno R. and Yokota H.; 2016: *Frequency dispersion compensation through variable window utilization in time-reversal techniques for electromagnetic waves*. IEEE Trans. Antennas Propag., 64, 3636-3639.

Abduljabbar A.M., Yavuz M.E., Costen F., Himeno R. and Yokota H.; 2017: *Continuous wavelet transform-based frequency dispersion compensation method for electromagnetic time reversal imaging*. IEEE Trans. Antennas Propag., 65, 1321-1329.

Annan A.P., Diamanti N., Redman J.D. and Jackson S.R.; 2016: *Ground-penetrating radar for assessing winter roads GPR for assessing winter roads*. Geophys., 81, WA101-WA109.

Arslan A.N., Wang H., Pulliainen J. and Hallikainen M.; 2001: *Effective permittivity of wet snow using strong fluctuation theory.* Prog. Electromagn. Res., 31, 273-290.

Artman B., Podladtchikov I. and Witten B.; 2010: *Source location using time-reverse imaging.* Geophys. Prospect., 58, 861-873.

Barone P.M. and Di Maggio R.M.; 2018: *Forensic investigations of geohazards: the Norcia 2016 earthquake.* Geosci., 8, 316.

Barone P.M. and Di Maggio R.M.; 2019: *Forensic geophysics: ground penetrating radar (GPR) techniques and missing persons investigations.* Forensic Sci. Res., 4, 337-340.

Bradford J.H. and Harper J.T.; 2005: *Wave field migration as a tool for estimating spatially continuous radar velocity and water content in glaciers.* Geophys. Res. Lett., 32, L08502, 4 pp., doi: 10.1029/2004GL021770.

Bradford J.H., Harper J.T. and Brown J.; 2009: *Complex dielectric permittivity measurements from ground-penetrating radar data to estimate snow liquid water content in the pendular regime.* Water Resour. Res., 45, W08403, 12 pp., doi: 10.1029/2008WR007341.

Bradford J.H., Privette J., Wilkins D. and Ford R.; 2018: *Reverse-time migration from rugged topography to image ground-penetrating radar data in complex environments.* Eng., 4, 661-666.

Braga I.L.S. and Moraes F.S.; 2013: *High-resolution gathers by inverse Q filtering in the wavelet domain.* Geophys., 78, V53-V61.

Chen S.Y., Chew W.C., Santos V.R.N., Sainath K. and Teixeira F.L.; 2016: *Electromagnetic subsurface remote sensing.* In: Wiley Encyclopedia of Electrical and Electronics Engineering, John Wiley and Sons, Hoboken, NJ, USA, 28 pp., doi: 10.1002/047134608X.W3602.pub2.

Colbeck S.C.; 1997: *A review of sintering in seasonal snow.* US Army Corps of Engineers, Cold Regions Research & Engineering Laboratory, Hanover, NH, USA, CRREL Report 97-10, 17 pp.

Denoth A.; 2003: *Structural phase changes of the liquid water component in Alpine snow*. Cold Reg. Sci. Technol., 37, 227-232.

Ebrahimi A., Gholami A. and Nabi-Bidhendi M.; 2017: *Sparsity-based GPR blind deconvolution and wavelet estimation*. J. Ind. Geophys. Union., 21, 7-12.

Ebrahimy A., Ghanbari S. and Ashtari A.; 2012: *FDTD numerical GPR stratigraphy modeling and processing and a case study with GPR data.* In: Abstracts International Geophysical Conference and Oil & Gas Exhibition, Istanbul, Turkey, Society of Exploration Geophysicists and The Chamber of Geophysical Engineers of Turkey, 4 pp., doi: 10.1190/IST092012-001.123.

Farge M.; 1992: *Wavelet transforms and their applications to turbulence.* Annu. Rev. Fluid Mech., 24, 395-458.

Fink M.; 1992: *Time reversal of ultrasonic fields. I. Basic principles.* IEEE Trans. Ultrason. Ferroelectr. Freq. Control, 39, 555-566, doi: 10.1109/58.156174.

Fink M., Prada C., Wu F. and Cassereau D.; 1989: *Self-focusing in inhomogeneous media with time reversal acoustic mirrors.* In: Proc. IEEE Ultrasonics Symposium, Montreal, QC, Canada, pp. 681-686, doi: 10.1109/ULTSYM.1989.67072.

Fink M., Cassereau D., Derode A., Prada C., Roux P., Tanter M. and Wu F.; 2000: *Time-reversed acoustics.* Rep. Prog. Phys., 63, 1933-1995, doi: 10.1088/0034-4885/63/12/202.

Forbes S.L., Hulsman S. and Dolderman M.; 2013: *Locating buried canine remains using ground penetrating radar*. Can. Soc. Forensic Sci. J., 46, 51-58.

Fouda A.E., Teixeira F.L. and Yavuz M.E.; 2012: *Time reversal techniques for MISO and MIMO wireless communication systems.* Radio Sci., 47, RS0P02, 15 pp., doi: 10.1029/2012RS005013.

Gabriel C., Gabriel S. and Corthout Y.E.; 1996a: *The dielectric properties of biological tissues: I. Literature survey.* Phys. Med. Biol., 41, 2231-2249, doi: 10.1088/0031-9155/41/11/001.

Gabriel S., Lau R.W. and Gabriel C.; 1996b: *The dielectric properties of biological tissues: II. Measurements in the frequency range 10 Hz to 20 GHz.* Phys. Med. Biol., 41, 2251-2269, doi: 10.1088/0031-9155/41/11/002.

Galley R.J., Trachtenberg M., Langlois A., Barber D.G. and Shafai L.; 2009: *Observations of geophysical and dielectric properties and ground penetrating radar signatures for discrimination of snow, sea ice and freshwater ice thickness.* Cold Reg. Sci. Technol., 57, 29-38.

Ghanbari S. and Hafizi M.K.; 2013: *The effect of antenna central frequency and application of advanced processing in locating buried urban utilities by GPR method.* Iranian Geophysics Journal, 7, 93-106.

Ghanbari S. and Hafizi M.K.; 2016: *Application of forward modelling and processing algorithm in Ghanat detection by GPR.* Iran. J. Geophys., 10, 67-82.

Ghanbari S., Hafizi M.K. and Bano M.; 2021: *Investigation of the application of wavelet transform to Geo-Radar with a case study of forensic geophysics in snow.* Iran. J. Geophys., 15, 91-110.

Ghanbari S., Hafizi M.K., Bano M. and Ebrahimi A.; 2022a: *Application of time-reversal (TR) imaging to GPR data for detecting an avalanche victim*. Arabian J. Geosci., 15, 11 pp., doi: 10.1007/s12517-022-09722-y.

Ghanbari S., Hafizi M.K., Bano M., Ebrahraimi A. and Hosseinzadeh N.; 2022b: *An enhanced GPR-based data processing approach for detecting subsurface utilities in urban distribution networks.* J. Appl. Geophys., 207, 104831, 13 pp., doi: 10.1016/j.jappgeo.2022.104831.

Greene E.M., Birkeland K.W., Elder K., Johnson G., Landry C., McCammon I., Moore M., Sharaf D., Sterbenz C., Tremper B. and Williams K.; 2004: *New observation guidelines for Avalanche programs in the United States.* In: Proc. 2004 International Snow Science Workshop, Jackson Hole, WY, USA, American Avalanche Association, Pagosa Springs, CO, USA, pp. 161-164.

Hammon III W.S., McMechan G.A. and Zeng X.; 2000: *Forensic GPR: finite-difference simulations of responses from buried human remains.* J. Appl. Geophys., 45, 171-186.

Jazayeri S., Ebrahimi A. and Kruse S.; 2017: *Sparse blind deconvolution of common-offset GPR data.* In: SEG Technical Program Expanded Abstracts 2017, Society of Exploration Geophysicists, Houston, TX, USA, pp. 5140-5145, doi: 10.1190/segam2017-17791251.1.

Lin S.C. and Too G.P.; 2014: *Application of array microphone measurement for the enhancement of sound quality by use of adaptive time reversal method.* Sens. Actuators, A, 218, 1-9.

Liu Z., Xu Q., Gong Y., He C. and Wu B.; 2014: *A new multichannel time reversal focusing method for circumferential Lamb waves and its applications for defect detection in thick-walled pipe with large-diameter*. Ultrason., 54, 1967-1976.

Marshall H.P., Koh G. and Forster R.R.; 2005: *Estimating alpine snowpack properties using FMCW radar.* Ann. Glaciol., 40, 157-162.

Mora N., Rachidi F. and Rubinstein M.; 2012: *Application of the time reversal of electromagnetic fields to locate lightning discharges.* Atmos. Res., 117, 78-85.

Morlet J., Arens G., Fourgeau E. and Glard D.; 1982: *Wave propagation and sampling theory—Part I: Complex signal and scattering in multilayered media.* Geophys., 47, 203-221.

Pethig R.; 1985: *Dielectric and electrical properties of biological materials.* J. Bioelectr., 4, vii-ix, doi: 10.3109/15368378509033258.

Petromichelakis I., Tsogka C. and Panagiotopoulos C.G.; 2018: *Signal-to-Noise Ratio analysis for time-reversal based imaging techniques in bounded domains.* Wave Motion, 79, 23-43.

Sandmeier K.J.; 2012: *REFLEXW Version 7.0, Program for the processing of seismic, acoustic or electromagnetic reflection, refraction and transmission data.* User's Manual, Karlsruhre, Germany, 578 pp.

Santos V.R.N. and Teixeira F.L.; 2017: *Application of time-reversal-based processing techniques to enhance detection of GPR targets.* J. Appl. Geophys., 146, 80-94.

Schwan H.P. and Li K.; 1953: *Capacity and conductivity of body tissues at ultrahigh frequencies.* Proc. IRE, 41, 1735-1740, doi: 10.1109/JRPROC.1953.274358.

Sihvola A. and Tiuri M.; 1986: *Snow fork for field determination of the density and wetness profiles of a snow pack.* IEEE Trans. Geosci. Remote Sens., GE-24, 717-721, doi: 10.1109/TGRS.1986.289619.

Sun M., Pan J., Le Bastard C., Wang Y. and Li J.; 2019: *Advanced signal processing methods for ground-penetrating radar: applications to civil engineering.* IEEE Signal Process. Mag., 36, 74-84.

Taflove A. and Hagness S.; 2005: *Computational Electrodynamics: the Finite-Difference Time-Domain Method, Third Edition.* Artech House, Boston, USA, 1038 pp.

Tiuri M., Sihvola A., Nyfors E.G. and Hallikaiken M.; 1984: *The complex dielectric constant of snow at microwave frequencies.* IEEE J. Oceanic Eng., 9, 377-382.

Torrence C. and Compo G.P.; 1998: *A practical guide to wavelet analysis.* Bull. Am. Meteorol. Soc., 79, 61-78.

Turner G. and Siggins A.F.; 1994: *Constant Q attenuation of subsurface radar pulses.* Geophys., 59, 1192-1200.

Ulaby F.T., Michielssen E. and Ravaioli U.; 2010: *Fundamentals of applied electromagnetics 6 ed*. Prentice Hall, Boston, MA, USA, 146 pp.

Wang Y.; 2006: *Inverse Q-filter for seismic resolution enhancement.* Geophys., 71, V51-V60.

Yao G.; 2013: *Least-squares reverse-time migration.* Ph.D. Thesis, Department of Earth Science and Engineering, Imperial College London, London, England, 193 pp., doi: 10.25560/14575.

Yavuz M.E. and Teixeira F.L.; 2005: *A numerical study of time-reversed UWB electromagnetic waves in continuous random media.* IEEE Antennas Wirel. Propag. Lett., 4, 43-46.

Yavuz M.E. and Teixeira F.L.; 2006: *Full time-domain DORT for ultrawideband electromagnetic fields in dispersive, random inhomogeneous media.* IEEE Trans. Antennas Propag., 54, 2305-2315.
Yavuz M.E. and Teixeira F.L.; 2009: *Ultra wideband microwave sensing and imaging using time-reversal techniques: a review.* Remote Sens., 1, 466-495, doi: 10.3390/rs1030466.
Yavuz M.E., Fouda A.E. and Teixeira F.L.; 2014: *GPR signal enhancement using sliding-window space-frequency matrices.* Progr. Electromagn. Res., 145, 1-10, doi: 10.2528/PIER14010105.

Corresponding author: Sajjad Ghanbari
Faculty of Science, Razi University
Zakariya Razi Blvd., Kermanshah, Iran
Phone: +98 83 34277605; e-mail: sajjad.ghanbari@alumni.ut.ac.ir

Appendix

The determination of wave propagation velocity can be achieved by analysing diffraction hyperbolas, as exemplified in the research conducted by Bradford and Harper (2005) and Ghanbari and Hafizi (2013).

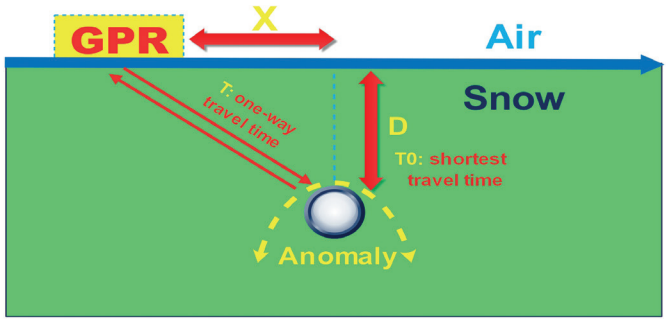

Fig. A1 - A GPR wave propagation model employing a hyperbolic diffraction model for the precise targeting of a specific object.

The wave velocity can be determined by fitting a curve to the diffraction hyperbolic event in the radargram, as illustrated in Fig. A1. This fitting process is performed using the two equations provided below (Bradford and Harper, 2005):

$$V = \sqrt{\frac{X^2\left(T^2+T_0^2\right)+2X\sqrt{T^2T_0^2\left(X^2+D^2\right)-\left(T^4+T_0^4\right)}}{\left(T^2-T_0^2\right)}} \tag{A1}$$

if

$$D = \frac{T_0 X}{\sqrt{T^2-T_0^2}} = \frac{X}{\sqrt{\left(T^2/T_0^2\right)-1}} \Longrightarrow V = \frac{X}{\sqrt{\left(T^2-T_0^2\right)}}. \tag{A2}$$

In the context of GPR analysis, the one-way travel time (T) of the GPR wave to the anomaly is determined, along with the shortest travel time (T_0) measured at the top of the anomaly. Additionally, the known depth (D) of the anomaly, together with its horizontal separation (X) from the GPR antenna, are taken into account.